

# Unzipping Long Valley: An explanation for vent migration patterns during an elliptical ring fracture eruption

Eoghan P. Holohan\* } Department of Geology, School of Natural Sciences, Trinity College, Dublin 2, Ireland  
 Valentin R. Troll }

Benjamin van Wyk de Vries Laboratoire Magmas et Volcans, 5 rue Kessler, 63038 Clermont-Ferrand, France

John J. Walsh Fault Analysis Group, School of Geological Sciences, University College Dublin, Dublin 4, Ireland

Thomas R. Walter GFZ Potsdam, Telegrafenberg, Potsdam, D-14473, Germany

## ABSTRACT

**Long Valley caldera, California, formed during the cataclysmic Pleistocene eruption of the Bishop Tuff. Previous stratigraphic and petrologic studies of this eruption deciphered an intriguing pattern of vent migration, thought to mirror the lateral propagation (“unzipping”) of magma-tapping ring fractures during caldera collapse. From scaled analog models, we show that this unzipping pattern was intrinsically related to the high plan-view ellipticity of the precollapse magma chamber roof. We also provide a first-order kinematic explanation for the systematic location of initial elliptical roof failure and for the lateral propagation of highly elliptical ring fractures.**

**Keywords:** Long Valley caldera, subsidence, ring structures, volcanoes, tectonics.

## INTRODUCTION

The 760,000 yr B.P. Bishop Tuff eruption from the resurgent Long Valley caldera, California, was the third largest volcanic outburst in Pleistocene North America (Mason et al., 2004). In under a week, some 700 km<sup>3</sup> (bulk volume) of rhyolite erupted, and the magma chamber roof subsided by 2–3 km (Hildreth and Wilson, 2007, and references therein). This formed a highly elliptical (32 × 16 km) caldera, around which >200 km<sup>3</sup> of ignimbrite buried an area of >2200 km<sup>2</sup> (Fig. 1A). Also, ~250 km<sup>3</sup> of ash fall blanketed >8,100,000 km<sup>2</sup> from California to Kansas (Hildreth and Wilson, 2007).

Hildreth and Mahood (1986) and Wilson and Hildreth (1997) constrained the temporal and spatial evolution of Bishop Tuff vents through detailed petrologic, lithologic, and stratigraphic studies of successively erupted extra-caldera deposits. On the caldera’s southern side, early fall deposits hosting lithics from Mount Morrison Pendant metasediments and Wheeler Crest Monzonite only (Fig. 1B) point to a Plinian column in the SSE. Ig1E is coeval with these fall units; similar lithic suites indicate a similar vent location. The overlying Ig2E displays marked up-section increases in the proportion of Glass Mountain rhyolite lithics, however. This reflects vent migration and ring fracture propagation from the SSE to the E (Wilson and Hildreth, 1997) (Fig. 1C). Granodiorite fragments (Hildreth and Mahood, 1986) suggest fracture propagation to the SW also. Significantly, Glass Mountain clasts in Ig2E are typically weathered and rounded; fresh angular rhyolite is rare. The ring fracture thus passed through Glass Mountain’s volcanoclastic apron, but not into the Glass

Mountain edifice (i.e., did not cross the caldera’s long axis; Wilson and Hildreth, 1997) (Fig. 1C).

On the caldera’s northern side, Ig2NW slightly predates Ig2N. Metamorphic and basalt fragments are abundant in Ig2NW, granitoid and quartz-latte lithics are rare, and Glass Mountain rhyolite lithics are absent. This constrains the earliest northern Ig2 vents to the area S or SW of Bald Mountain (Wilson and Hildreth, 1997) (Figs. 1B and 1C). In Ig2N, Glass Mountain

rhyolite lithics dominate, however, and many in upper Ig2N are fresh and angular. Ring fracture propagation was thus from the NNW, to the NE, and through the Glass Mountain edifice (Wilson and Hildreth, 1997) (Fig. 1).

Two separate ring fractures hence formed simultaneously in the N and S of the collapsing caldera, and propagated toward the E (and W?; Fig. 1), but reasons for this peculiar pattern of ring fracture “unzipping” were unclear (Wilson and Hildreth, 1997). Intriguingly, Roche et al. (2000) noted similar ring fracture development in a physical model of a subsiding reservoir roof that had an elliptical plan-view shape. This result was unexplained, however. We present new physical modeling data that systematically illustrate how a range of magma chamber plan-view ellipticities may affect patterns of ring fracture localization and propagation during roof subsidence. We also provide a mechanical rationale for such unzipping patterns in the models, at Long Valley caldera, and elsewhere.

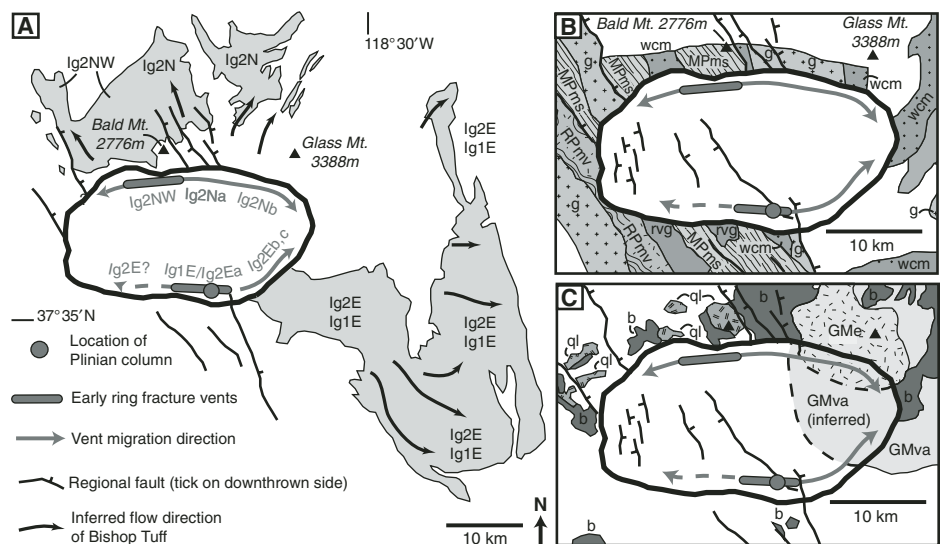


**Figure 1. A: Map of Long Valley caldera and Bishop Tuff outcrop, with inferred migration pattern of ring fracture vents for successive ignimbrite packages. Two main ignimbrites, an earlier “Ig1” and a later “Ig2”, were erupted. Letters E, N, and NW denote the extra-caldera sector in which an ignimbrite is found; letters a, b, and c denote ignimbrite sub-packages up-section. B: Precaldera basement rocks. C: Precaldera volcanic rocks (modified from Hildreth and Mahood, 1986, and Wilson and Hildreth, 1997). MPms—Mount Morrison Pendant metasediments; Rpmv—Ritter Pendant metavolcanics; wcm—Wheeler Crest Monzonite; rvg—Round Valley Peak Granodiorite; g—other granitoids; b—basalt; ql—quartz-latte; GMva—Glass Mountain volcanoclastic apron; GMme—Glass Mountain edifice.**

\*E-mail: holohane@tcd.ie

## PHYSICAL MODELS

### Setup and Scaling

Each model (Fig. 2) comprised a 2-cm-thick, sill-like reservoir of creamed honey within a pack of sand and gypsum (mixed 4:1 by volume). A 0.8 cm diameter honey conduit allowed evacuation of the reservoir from its base. The ratio of the reservoir's horizontal long and short axes,  $A/B$ , defines the roof's plan-view ellipticity. Four model types were run:  $A/B = 1.0$ ,  $A/B = 1.3$ ,  $A/B = 1.5$ , and  $A/B = 2.0$  (Fig. 2). Each type was run five times to ensure reproducibility of results, and additional models tested the results' sensitivity to the conduit's lateral position.

The length ratio,  $l^* = l_{\text{model}}/l_{\text{nature}}$ , was  $5 \times 10^{-6}$ , so 1 cm in the models scales to  $\sim 2$  km in nature. The  $\sim 14 \times 7$  cm model reservoirs ( $A/B = 2.0$ ) thus approximate the  $\sim 32 \times 16$  km Long Valley caldera, and their 3 cm depth corresponds to the  $\sim 5$ – $6$  km pre-eruptive depth of the Bishop Tuff reservoir (Anderson et al., 2000). Stress or cohesion ( $\sigma$ ), density ( $\rho$ ), and gravity ( $g$ ) ratios relate through  $\sigma^* = \rho^*g^*l^*$  (cf. Roche et al., 2000). Since  $\rho_{\text{model}} = 1400 \text{ kg m}^{-3}$  and  $\rho_{\text{nature}} \approx 2800 \text{ kg m}^{-3}$  (Goodman, 1989),  $\rho^* = 0.5$ . Since  $g_{\text{model}} = g_{\text{nature}}$ ,  $g^* = 1$ . The cohesion ratio was thus  $\sigma^* = 2.5 \times 10^{-6}$ . Cohesion of pristine natural rock is  $10^5$ – $10^8$  Pa (cf. Schellart, 2000), and perhaps  $\sim 10^6$  Pa with mechanical anisotropy (fractures, etc.; Schultz, 1996). The required model cohesion was thus 0.25–250 Pa. At model normal stresses, cohesion of dry, fine-grained sand is 0–250 Pa (Schellart, 2000); addition of finer material such as gypsum raises this value only slightly (e.g.,  $\sigma_{\text{model}} \approx 200$  Pa in Donnadieu and Merle, 1998). The internal friction angles of sand/gypsum and natural rocks match:  $\phi_{\text{model}} \approx 37^\circ$ ,  $\phi_{\text{nature}} = 30^\circ$ – $45^\circ$  (Schellart, 2000).

Viscosity ( $\eta$ ), stress ( $\sigma$ ), and time ( $T$ ) ratios relate through  $\eta^* = \sigma^*T^*$  (cf. Donnadieu and Merle, 1998). The time ratio is  $T^* = l^*/V^*$ , where  $V$  is velocity. Natural and model collapse velocities of  $\sim 1$  km per day and  $\sim 0.5$  cm per hour give  $V^* = 1.2 \times 10^{-4}$ . Since  $l^* = 5 \times 10^{-6}$ ,  $T^* = 4.2 \times 10^{-2}$ . A median honey viscosity of 400 Pa s thus scales to  $\eta_{\text{nature}} = 3.8 \times 10^9$  Pa s.

With a temperature of 700–800 °C, crystal content of 1–25 vol%, and  $\text{H}_2\text{O}$  content of 4–6 wt% (Anderson et al., 2000; Hildreth and Wilson, 2007), erupted Bishop rhyolite viscosity was probably  $\sim 10^5$ – $10^7$  Pa s (Wolff et al., 1990; Dingwell, 1999). When its mushy to semi-solidified margins (Hildreth and Wilson, 2007, p. 982) are also considered, however, the Bishop reservoir's bulk viscosity was likely much higher, and the honey may approximate this. For further details of model construction and scaling, see Holohan et al. (2008).

### Results

All model collapses began with sagging about the roof's center and surficial tension cracking at its margins (Fig. 3, Ai–Di). Tension cracks were often more marked around the ends of elliptical roofs' short axes. Complete roof failure always occurred with localization of a steeply outward-dipping reverse fault (note snubbed scarps in Fig. 3, Aii–Dii; Fig. 4A). For circular roofs, the localization of the first reverse fault was apparently random, but for elliptical roofs, reverse faults *always* first localized around the ends of the reservoir's short axis (Fig. 3, Aii–Dii).

Patterns of reverse fault localization and lateral propagation (“unzipping”) constituted a continuum bound by end members characteristic of the  $A/B = 1$  (circular) and  $A/B = 2$  (highly elliptical) roof geometries. Circular reservoir roofs usually displayed unzipping *pattern 1* (Fig. 3, Ai–Aiv), whereby the reverse fault first localized at one side of the reservoir and then propagated bidirectionally around to a “hinge zone” on the opposite side. Slightly elliptical roofs ( $A/B = 1.33$ ) often displayed the bidirectional unzipping *pattern 1* (Fig. 3, Bi–Biv), like the circular case, or else *pattern 2* (Fig. 3, Ci–Civ), where the reverse fault propagated mainly unidirectionally from one end of the roof's short axis, around the long axis, and past the other short-axis end. Moderately elliptical roofs ( $A/B = 1.5$ ) displayed unzipping *pattern 2* or else *pattern 3* (Fig. 3, Di–Div), where two discrete reverse faults localized simultaneously or in quick succession, one around each end of the roof's short axis. Both reverse faults then propagated bidirectionally to, and usually linked at, the ends of the roof's long axis. Highly elliptical roofs ( $A/B = 2.0$ ) displayed unzipping *pattern 3* only.

Just after or synchronous with reverse faulting, inward-dipping normal faults (kinematically linked to the reverse faults; cf. Roche et al., 2000) formed within the marginal zone of early surficial tensile fractures. At high plan-view ellipticities ( $A/B = 2.0$ ), normal fault unzipping (“onf” in Fig. 3) usually mimicked that of the reverse faults.

Only once, with a circular roof, did a reverse ring fault localize instantaneously all around a reservoir circumference (*pattern 0*, “no unzip-

ping”; Appendix DR1<sup>1</sup>). With centrally sited or laterally sited conduits, patterns of sagging, reverse fault localization, and “unzipping” were essentially the same (Appendix DR2). This precludes any major influence from the conduit position on these patterns, and shows that they are primarily governed by roof geometry.

### MECHANICAL RATIONALE

In experiment, the reservoir roof initially undergoes centroclinal sagging and ultimately fails along a shear fracture that dips outward with a reverse sense of slip. This shear fracture is in Riedel orientation, and localizes with sufficient vertical shear strain ( $\gamma$ )—or angular shear ( $\psi$ ), since  $\gamma = \tan \psi$ —between the down-going roof and its comparatively unaffected surroundings (cf. Roche et al., 2000) (Fig. 4C).

For a circular reservoir roof, net angular shear and shear strain from the roof center to the unaffected surroundings should be equal on all cross sections. This is because the vertical displacement at the roof center is accommodated over the same horizontal distance on any line of section. The locus of initial failure in circular roofs should thus ideally occur as a complete ring, but with subtle anisotropies in roof loading it may instead occur as an apparently randomly located arc (Fig. 3, Aii).

In an elliptical roof, however,  $\gamma$  and  $\psi$  are at a maximum along the roof's short axis, since here the vertical displacement at the roof center is accommodated over the shortest horizontal distance. Conversely,  $\gamma$  and  $\psi$  are at a minimum along the roof's long axis (Fig. 4C versus Fig. 4D). Angular shear along either axis peaks at the zone of maximum angular deflection of the roof from horizontal. This zone occurs just inside the reservoir margin, around the inflection points of the roof's deflection profile (Figs. 4C and 4D). As they are proportional to the net angular shear, peak angular shear and peak shear strain are also greatest along the short axis. Complete failure of a down-warped elliptical roof via a shear fracture therefore first occurs along, and near the end of, the roof's shorter principal axis (Fig. 4C versus Fig. 4D), and proceeds from there toward the long axis.

As the  $A/B$  ratio increases, for a given central subsidence, shear strain is increasingly greater on a roof's short axis than on its long axis. At intermediate  $A/B$  ratios (1.33–1.5), this disparity may be low enough to allow subtle anisotropies in roof load to shift subsidence slightly toward one end of the short axis to produce unzipping *pattern 1*, or toward one end of the long axis to produce unzipping *pattern 2*. At high  $A/B$  ratios

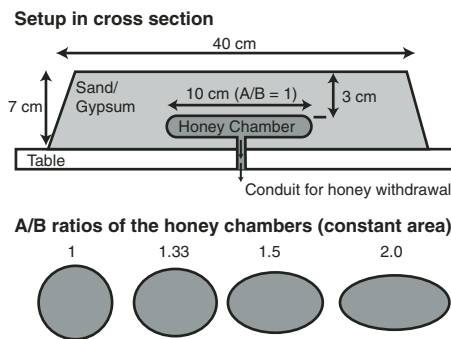


**Figure 2.** Sketch cross section of experiment setup.

<sup>1</sup>GSA Data Repository item 2008075, Appendices 1 and 2 (full experimental unzipping data sets), is available online at [www.geosociety.org/pubs/ft2008.htm](http://www.geosociety.org/pubs/ft2008.htm), or on request from [editing@geosociety.org](mailto:editing@geosociety.org) or Documents Secretary, GSA, P.O. Box 9140, Boulder, CO 80301, USA.

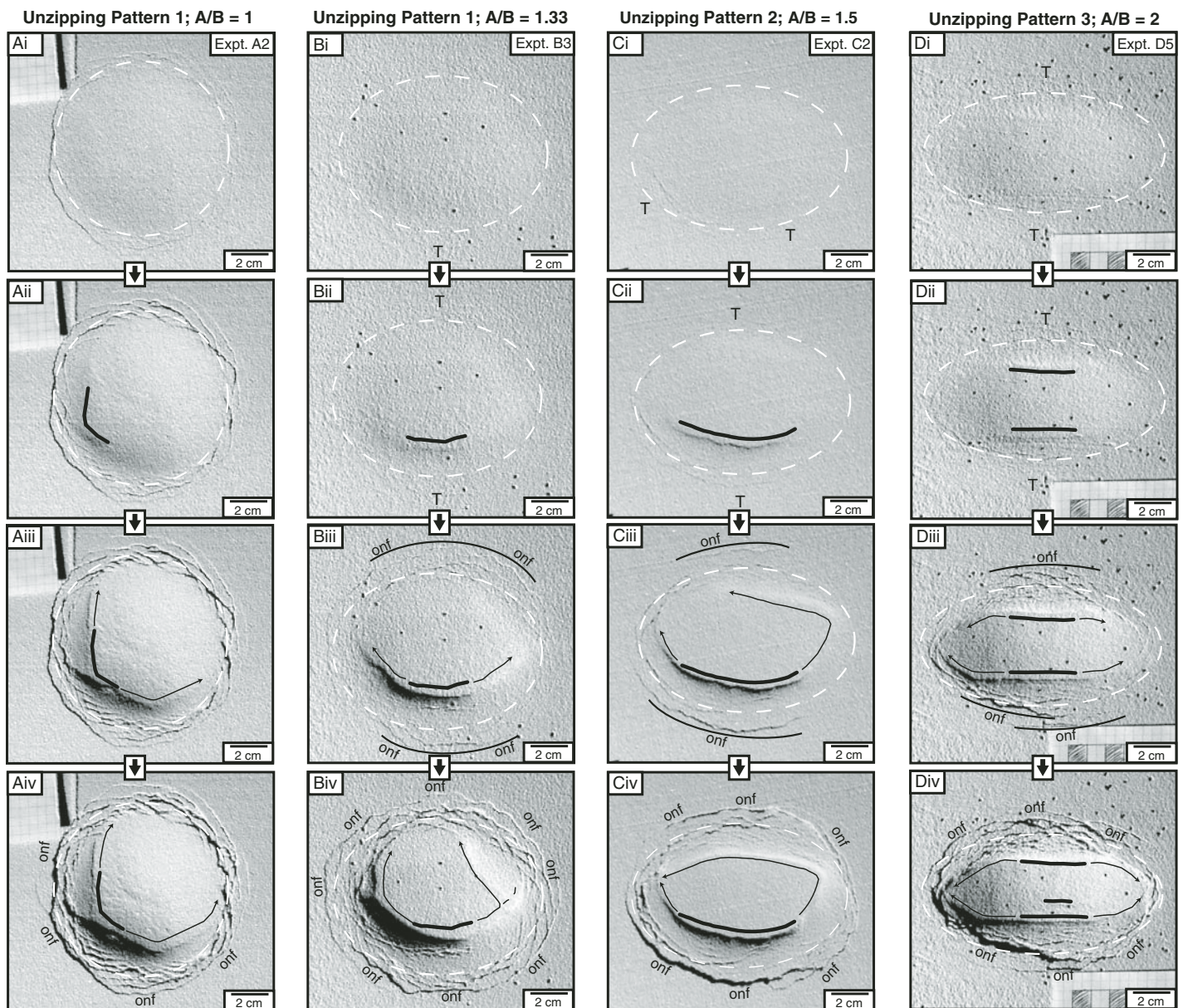


**Figure 3.** Time-lapse photos of experimental caldera collapses. These represent the main unzipping patterns observed, but note that  $A/B = 1.33$  produced patterns 1 or 2, while  $A/B = 1.5$  produced patterns 2 or 3. See Appendices for full data set. Ai–Di: prefailure sagging and surficial tension cracks (T). Dashed white line is approximate chamber outline at depth. Aii–Dii: Localization of inner reverse fault(s) (trace indicated by thick black line). Aiii–Diii: Lateral propagation of reverse fault trace(s), tracked by thin black line and arrows. Also see onset of outer normal faulting (onf—medium black lines). Aiv–Div: Completion of ring fault propagation.

( $\sim 2.0$ ), however, the shear strain disparity is so great that two discrete reverse faults always rapidly nucleate along the roof's short axis, one at each end, before propagating laterally toward the long axis—as occurred at Long Valley caldera.

## DISCUSSION

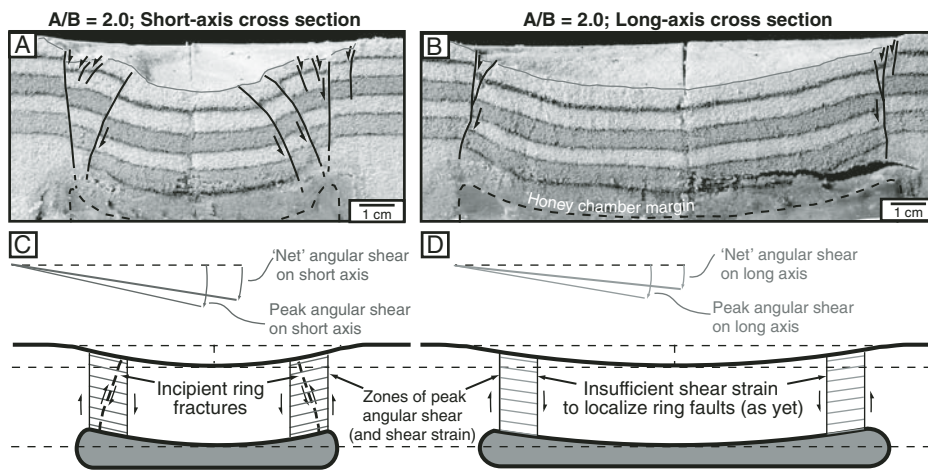
Analytical solutions used by engineers to calculate deflection profiles and stresses arising in uniformly loaded, elliptical or rectangular, elastic plates—similar to gravitationally-loaded, elongate magma chamber roofs—lead to conclusions similar to those from our experimental results (Timoshenko and Woinowsky-Krieger, 1959; Sato, 2006). With relatively restrained

plate edges, such as would be expected for a magma chamber roof, these solutions predict down-flexure toward the plate's center, with maximum angular deflections, shear strains, and shear stresses near the ends of the plate's short axis. Predicted bending stresses and marginal tensile reactions to central down-flexure also peak along the plate's short axis. This may explain the typical initiation and greater intensity of tensile fractures and normal faults here in experiment (cf. Fig. 3, and Fig. 4A versus Fig. 4B).

Such analytical solutions apply most rigorously to relatively thin plates, but boundary element models of surface subsidence profiles above depressurized, elliptical, and “thick-

roofed” hydrocarbon reservoirs (Gambolati et al., 1987) also broadly agree with our experimental profiles. Furthermore, observed “real-time” surface subsidence profiles and fracture patterns related to *upward* fluid extraction at elliptical oil fields, e.g., Wilmington oil field, California ( $16 \times 6$  km; Allen, 1968), and Goose Creek oil field, Texas ( $3.5 \times 2.2$  km; Yerkes and Castle, 1976), mimic those in experiment. These observations with different fluid extraction directions further support the transferability of our model results to nature.

Wilson and Hildreth (1997, p. 436) speculated that a “line of weakness” may have localized the points of initial ring fracturing at Long



**Figure 4. A and B: Cross sections through the  $A/B = 2.0$  elliptical collapse model. Note that along the short axis, shear fractures accommodate more of the central vertical displacement. C and D: Sketch cross sections of *prefailure* deflection profiles along the short and long axes of an elliptical magma chamber roof. Profiles are based on prefailure surface deflections in experiment (cf. Fig. 3, Di). Deflection angles are shown over same horizontal length to ease visual comparison. Greatest angular shear, and hence shear strain, along the short axis leads to earliest shear failure here.**

Valley, since the early N and S vents seem aligned along the main NW-SE regional fault trend. The NW-SE faults cannot have readily caused the ring fractures' W-E propagation, however, although Lavallée et al. (2004) suggested that a topographic load from Glass Mountain (Fig. 1) might have done so. Such factors may have exerted some complementary influences on the pattern of ring fault development, but we argue that they were secondary to the reservoir roof's high ellipticity (from caldera dimensions,  $A/B \geq 2.0$ ), a factor that our models show could by itself produce *both* the localization *and* the propagation of ring fractures inferred for the Bishop Tuff eruption.

Syn-collapse vent migration is also inferred around the end of the short axis of Laacher See depression, Germany ( $3.5 \times 2.5$  km; Van den Bogaard and Schmincke, 1984). Intermediate-size elliptical calderas, such as Campi Flegrei, Italy ( $17 \times 11.5$  km; Rosi et al., 1996), Rabaul, Papua New Guinea ( $14 \times 8$  km; Nairn et al., 1995), Suswa, Kenya ( $11 \times 8.6$  km; Skilling, 1993), and Alcedo, Galápagos Islands ( $8 \times 5.5$  km; Geist et al., 1994), host(ed) major vents near the ends of their short axis. The plan-view ellipticity of a magma chamber roof may thus decisively influence the location and dynamics of ring fracturing and eruption at all scales in nature.

## CONCLUSIONS

The pattern of vent migration and ring fracture unzipping at Long Valley, and possibly at other highly elliptical calderas, relates to two interlinked factors: (1) the high ellipticity of the precollapse magma chamber roof, and (2) the occurrence, upon the onset of chamber depressurization and roof sagging, of maximum prefailure shear strain along the elliptical roof's

short axis. Seismic and geodetic data from around its short axis may thus be crucial for hazard assessment at an elliptical magmatic center.

## ACKNOWLEDGMENTS

We thank S. Jones, R. West, T. Druitt, and O. Roche for helpful discussions, and I. Bindeman and J. Wolff for thoughtful reviews. E.P.H. and V.R.T. thank Enterprise Ireland and Trinity College, Dublin, for financial support.

## REFERENCES CITED

- Allen, D.R., 1968, Physical changes of reservoir properties caused by subsidence and repressuring operations: *Journal of Petroleum Technology*, v. 20, p. 23–29.
- Anderson, A.T., Davis, A.M., and Lu, F., 2000, Evolution of the Bishop Tuff rhyolitic magma based on melt and magnetite inclusions and zoned phenocrysts: *Journal of Petrology*, v. 41, p. 449–473, doi: 10.1093/petrology/41.3.449.
- Dingwell, D.B., 1999, Granitic melt viscosities: *Geological Society [London] Special Publication* 168, p. 27–38.
- Donnadieu, F., and Merle, O., 1998, Experiments on the indentation process during cryptodome intrusions: New insights into Mount St. Helens deformation: *Geology*, v. 26, p. 79–82, doi: 10.1130/0091-7613(1998)026<0079:EOTIPD>2.3.CO;2.
- Gambolati, G., Sartoretto, F., Rinaldo, A., and Ricceri, G., 1987, A boundary element solution to land subsidence above 3-D gas/oil reservoirs: *International Journal for Numerical and Analytical Methods in Geomechanics*, v. 11, p. 489–502, doi: 10.1002/nag.1610110505.
- Geist, D., Howard, K.A., Jellinek, A.M., and Rayder, S., 1994, The volcanic history of Volcán Alcedo, Galápagos Archipelago: A case study of rhyolitic oceanic volcanism: *Bulletin of Volcanology*, v. 56, p. 243–260.
- Goodman, R.E., 1989, Introduction to rock mechanics: New York, John Wiley and Sons, 576 p.
- Hildreth, W., and Mahood, G.A., 1986, Ring-fracture eruption of the Bishop Tuff: *Geological Society of America Bulletin*, v. 97, p. 396–403, doi:

10.1130/0016-7606(1986)97<396:REOTBT>2.0.CO;2.

- Hildreth, W., and Wilson, C.J.N., 2007, Compositional zoning of the Bishop Tuff: *Journal of Petrology*, v. 48, p. 951–999.
- Holohan, E.P., van Wyk de Vries, B., and Troll, V.R., 2008, Analogue models of caldera collapse in strike-slip tectonic regimes: *Bulletin of Volcanology* (in press).
- Lavallée, Y., Stix, J., Kennedy, B., Richer, M., and Longpré, M.-A., 2004, Caldera subsidence in areas of variable topographic relief: Results from analogue modelling: *Journal of Volcanology and Geothermal Research*, v. 129, p. 219–236, doi: 10.1016/S0377-0273(03)00241-5.
- Mason, B.G., Pyle, D.M., and Oppenheimer, C., 2004, The size and frequency of the largest explosive eruptions on Earth: *Bulletin of Volcanology*, v. 66, p. 735–748, doi: 10.1007/s00445-004-0355-9.
- Nairn, I.A., McKee, C.O., Talai, B., and Wood, C.P., 1995, Geology and eruptive history of Rabaul caldera area, Papua New Guinea: *Journal of Volcanology and Geothermal Research*, v. 69, p. 255–284.
- Roche, O., Druitt, T.H., and Merle, O., 2000, Experimental study of caldera formation: *Journal of Geophysical Research*, v. 105, p. 395–416, doi: 10.1029/1999JB900298.
- Rosi, M., Vezzoli, L., Aleotti, P., and De Censi, M., 1996, Interaction between caldera collapse and eruptive dynamics during the Campanian ignimbrite eruption, Phlegraean Fields, Italy: *Bulletin of Volcanology*, v. 57, p. 541–554.
- Sato, K., 2006, Bending of an elastically restrained elliptical plate under the combined action of a lateral load and an in-plane force: *Japan Society of Mechanical Engineers International Journal*, v. 49, p. 130–137.
- Schellart, W.P., 2000, Shear test results for cohesion and friction coefficients for different granular materials: Scaling implications for their usage in analogue modelling: *Tectonophysics*, v. 324, p. 1–16, doi: 10.1016/S0040-1951(00)00111-6.
- Schultz, R.A., 1996, Relative scale and the strength and deformability of rock masses: *Journal of Structural Geology*, v. 18, p. 1139–1149, doi: 10.1016/0191-8141(96)00045-4.
- Skilling, I.P., 1993, Incremental caldera collapse of Suswa volcano, Gregory Rift Valley, Kenya: *Geological Society [London] Journal*, v. 150, p. 885–896.
- Timoshenko, S., and Woinowsky-Krieger, S., 1959, *Theory of plates and shells*: London, McGraw-Hill, 580 p.
- Van den Bogaard, P., and Schmincke, H.-U., 1984, The eruptive centre of the Late Quaternary Laacher See Tephra: *Geologische Rundschau*, v. 73, p. 933–980.
- Wilson, C.J.N., and Hildreth, W., 1997, The Bishop Tuff: New insights from eruptive stratigraphy: *Journal of Geology*, v. 105, p. 407–439.
- Wolff, J.A., Wörner, G., and Blake, S., 1990, Gradients in physical parameters in zoned felsic magma bodies: Implications for evolution and eruptive withdrawal: *Journal of Volcanology and Geothermal Research*, v. 43, p. 37–55.
- Yerkes, R.F., and Castle, R.O., 1976, Seismicity and faulting attributable to fluid extraction: *Engineering Geology*, v. 10, p. 151–167, doi: 10.1016/0013-7952(76)90017-X.

Manuscript received 1 August 2007

Revised manuscript received 12 December 2007

Manuscript accepted 1 January 2008

Printed in USA